Lasers in Medical Science (2026) 41:215
https://doi.org/10.1007/s10103-026-05018-9

RESEARCH

Tumor border delineation in basal cell carcinoma using Fourier analysis

Luca Fésűs[1,2] · Fanni Meznerics[2] · András Bánvölgyi[2] · Norbert Wikonkál[2] · Róbert Szipőcs[1,3]

Received: 4 June 2026 / Accepted: 31 August 2026

Abstract

Basal cell carcinoma (BCC) is the most common malignancy in Caucasians. Surgical excision is the gold standard for treating BCC; however, poorly defined borders often challenge complete removal. Therefore, there is a need for efficient imaging techniques to enable visual and quantitative evaluation of BCC tumor borders before and during surgery. In this study, we aimed to develop a mathematical algorithm for tumor border delineation using nonlinear optical microscopy. Two-photon excitation auto-fluorescence (2PEF) and second-harmonic generation (SHG) images were acquired from nodular, micronodular, and infiltrative BCC skin sections. Fast Fourier transform (FFT) analysis was executed on two-dimensional SHG images, to characterize the collagen fibre structure. Based on differences in the collagen fiber network between healthy tissue and the tumor microenvironment, a heatmap was generated to visualize the predicted tumor borders of BCC skin sections. Spatial grid resolution proved to be a critical parameter for FFT analysis, with the highest border delineation accuracy achieved using a unit cell size of 0.14×0.14 mm². Smaller unit cells led to the omission of small tumor nests, whereas larger unit cells reduced sensitivity by including normal anatomical structures, such as hair follicles, within the predicted tumor border.

Keywords Nonlinear optical microscopy · Second harmonic generation · Fast Fourier transform · Basal cell carcinoma · Tumor border delineation · Collagen fiber analysis · Intraoperative diagnosis

Introduction

Basal cell carcinoma (BCC) is the most common malignancy in Caucasians. Although BCCs rarely metastasize, local tissue invasion may lead to severe health and cosmetic damage, and inoperability. The gold standard in the therapy of BCC is surgical excision. Clinicians, however, may encounter several challenges [1]. First, diagnosis of BCC cannot always be established solely based on physical and dermoscopic examination. Next, BCCs often have poorly defined borders that challenge complete surgical removal [2]. The growing need in oncology for label-free optical techniques for intraoperative tumor margin assessment is reflected in the rapid development of optical imaging devices and diagnostic algorithms [3]. Also, combination with AI may enable real-time diagnosis and intraoperative margin assessment, leading to a rapid and resource-efficient optical alternative for healthcare providers [4].

To date, the gold standard in the diagnosis of BCC is histopathology, which is largely based on hematoxylin and eosin (H&E) stained sections. Therefore, there is a demand

✉ Luca Fésűs
fesus.luca@semmelweis.hu

✉ Róbert Szipőcs
szipocs.robert@wigner.hu

Fanni Meznerics
meznerics.fanni.adel@semmelweis.hu

András Bánvölgyi
banvolgyi.andras@med.semmelweis-univ.hu

Norbert Wikonkál
wikonkal.norbert@med.semmelweis-univ.hu

1 Institute for Solid State Physics and Optics, HUN-REN Wigner RCP, Budapest, Hungary

2 Department of Dermatology, Venereology and Dermatooncology, Semmelweis University, Budapest, Hungary

3 R&D Ultrafast Lasers Ltd, Budapest, Hungary

Published online: 07 September 2026

for efficient imaging techniques for visualization of BCC cells and numerical evaluation of the tumor borders of BCC prior to and during surgery. Previous work observed an increased collagen fiber length, decreased fiber angle and significantly higher fiber alignment of collagen fibers in BCC with these techniques [5]. Nonlinear optical microscopy (NLM) including SHG and 2PEF has already been used in clinical settings too, to acquire images of BCCs from multiple depths [6]. In this study, morphological features of superficial, nodular and micronodular BCCs were described, mainly based on their 2PEF signal. Characteristic histological features of BCCs were revealed, although the lower penetration depth and lower field of view disabled the assessment of tumor border in case of thicker lesions and infiltrative BCCs. In another study, coherent anti-Stokes Raman scattering (CARS), SHG and 2PEF imaging was combined with Raman spectroscopy for morphological and chemical examination of BCC. The authors highlighted an increased intracellular lipid content in aggressive BCCs, although morphological assessment of tumor sites was challenging [7]. Another study combined diffuse reflectance spectroscopy with optical coherence tomography and high-frequency ultrasound to differentiate subtypes of basal cell carcinoma and benign neoplasms [8].

In this paper, we utilize second-harmonic generation (SHG) microscopy for mosaic imaging of the collagen structure of BCC skin samples and two-photon excitation fluorescence (2PEF) imaging to visualize keratin of the skin cells.We carried out fast Fourier transform (FFT) analysis on mosaic SHG images of skin sections from different BCC subtypes (nodular, micronodular and infiltrative BCC). Our aim was to investigate collagen structure in order to delineate tumor borders, and if possible, to differentiate between BCC subtypes. Our result shows that SHG images were suitable for FFT analysis, and in most BCC subtypes, tumor borders could be delineated. However, combination with 2PEF images is necessary, as small tumor nests and adnexal structures may distort the analysis.

Methods

For the SHG and 2PEF imaging, a fiber coupled version of our ~ 20 MHz repetition rate, tunable, sub-ps Ti: sapphire laser (*FemtoRose TUN LC GTI*, R&D Ultrafast Lasers Ltd., Budapest, Hungary, see Ref [9]. for details) was used with an operation wavelength set around ~ 800 nm. The relatively small ($\Delta\lambda \sim 1$ nm) spectral bandwidth of the laser allows distortion free fiber delivery of the optical pulses through a ~ 1.8 m long HC-800-2 type, commercial hollow core photonic bandgap fiber with honeycomb structure (product of NKT Photonics, Denmark [9]). Violet (405/20 nm) and orange (590/40 nm) band-pass emission filters were respectively installed to our LSM 7 MP microscope in order to spectrally select SHG and 2PEF signals. For focusing of the laser beam, a 20× water immersion objective (W-Plan – APOCHROMAT 20×/1,0 DIC (UV) VIS-IR, Carl Zeiss AG, Germany) was employed providing a field of view (FOV) of ~ 0.42 × 0.42 mm^2.

In this study, four nodular, four micronodular and four infiltrative BCC samples were analysed. The age of the patients was 67.6±16 (nodular BCC), 68.9±13.5 (micronodular BCC) and 69.7±12.2 (infiltrative BCC). Samples were formalin-fixed and paraffin-embedded, then 50 µm thick deparaffinized sections orthogonal to the skin surface were prepared.

FFT was carried out on mosaic SHG images of every BCC subtype to measure the degree of organization and symmetry of collagen fibers using a public domain image processing software (ImageJ) [10]. Individual FOVs (~ 0.42 × 0.42 mm^2) were divided into 4 (2 × 2), 9 (3 × 3), 16 (4 × 4) or 25 (5 × 5) even quadrangles (that we refer to as unit cells), for more precise spatial analysis. All unit cells with a total intensity above a certain threshold went through FFT analysis. As during imaging, rectangular areas are captured, empty FOVs appear at corners of the mosaic image, which are absent of any skin section. The raw intensity density value of these FOVs were used to determine our threshold value before FFT analysis. FFT output images were converted to power plots for more accurate analysis. As the eccentricity of the power plots reflect the arrangement of the collagen fibers, an ellipse was fitted to each power plot. We calculated collagen orientation (CO) index as the ratio of long-axis/short-axis of this ellipse. Previously CO index was used to describe collagen fiber morphology in healthy skin fibers exposed to load and collagen network around basal cell cancer nests [5, 11, 12]. Based on the axes of the ellipses gained from FFT transformation, a heatmap was created, where a higher longer/shorter axis ratio was and therefore was attributed red color. Maximum value of the CO index was truncated to 3 for better contrast in the corresponding heatmap. A circular power plot ($CO < 1.5$) reflects the isotropic behavior of „healthy collagen" in healthy skin and was displayed in blue. An elongated power plot ($CO > 2$) indicates parallelly oriented fibers, corresponding to collagen aligning the tumor nests and was displayed in red color. Heat map plots were generated by using MATLAB software.

Results

FFT analysis was carried out in four nodular, four micronodular and four infiltrative BCC skin sections. In all cases, every FOV was divided into smaller quadrangles, as described above. In Fig. 1, SHG and 2PEF mosaic image of a nodular

BCC is shown, with the outcome of multiple FFT analyses. On the multiphoton images (Fig. 1A), a large tumor mass is visible in the orange 2PEF channel that occupies the epidermis and dermis, surrounded by broad collagen fibers in the magenta SHG channel. Our result shows that accuracy of FFT analysis highly depends on the size of the analyzed FOVs. During the FFT analysis of different-sized quadrangles, we found that division of individual 0.42×0.42 mm^2 images to 9 (3×3) unit cells gave the best results regarding resolution and accuracy to highlight BCC tumor nests (see Fig. 1). When cells with smaller size were analyzed, differences between straight and curved fibers became less prominent. However, increasing the unit cell size does not improve predictive accuracy, as it results in the omission of small tumor nests inside the examined quadrangle (Fig. 1).

Although the infiltrative subtype was characterized by thick collagen bundles, setting unit cell size was challenging (data not shown). Applying a grid with high resolution again led to weaker accuracy, however, small tumor nests were omitted when unit cell size was increased.

A micronodular BCC is shown in Fig. 2. Small tumor nests are visible in the 2PEF channel, which are surrounded by broad, straight collagen fibers, compared to deeper regions of the dermis that contain healthy collagen. In the heatmap, not only the tumor border is indicated with high CO (red color), but the inner part of the tumor too, that corresponds to the micronodular histological subtype.

Our results indicate that thin collagen fibers are more difficult to analyze, which often results in false CO ratios (supporting data are omitted for brevity). We realized that small tumor nests have better visibility if they are surrounded by thicker collagen bundles. Large nodular BCCs are less accurately delineated in the heatmap, if the surrounding collagen fibers are thin, even if they are quite parallelly oriented.

An additional observation was that collagen fibers around hair follicles result in similar CO ratios as those around tumor nests (Fig. 3). To avoid misinterpretation, we used the 2PEF channel to differentiate between tumor nests and hair follicles. However, the SHG channel and the calculated CO alone is not indicative for the tumor border.

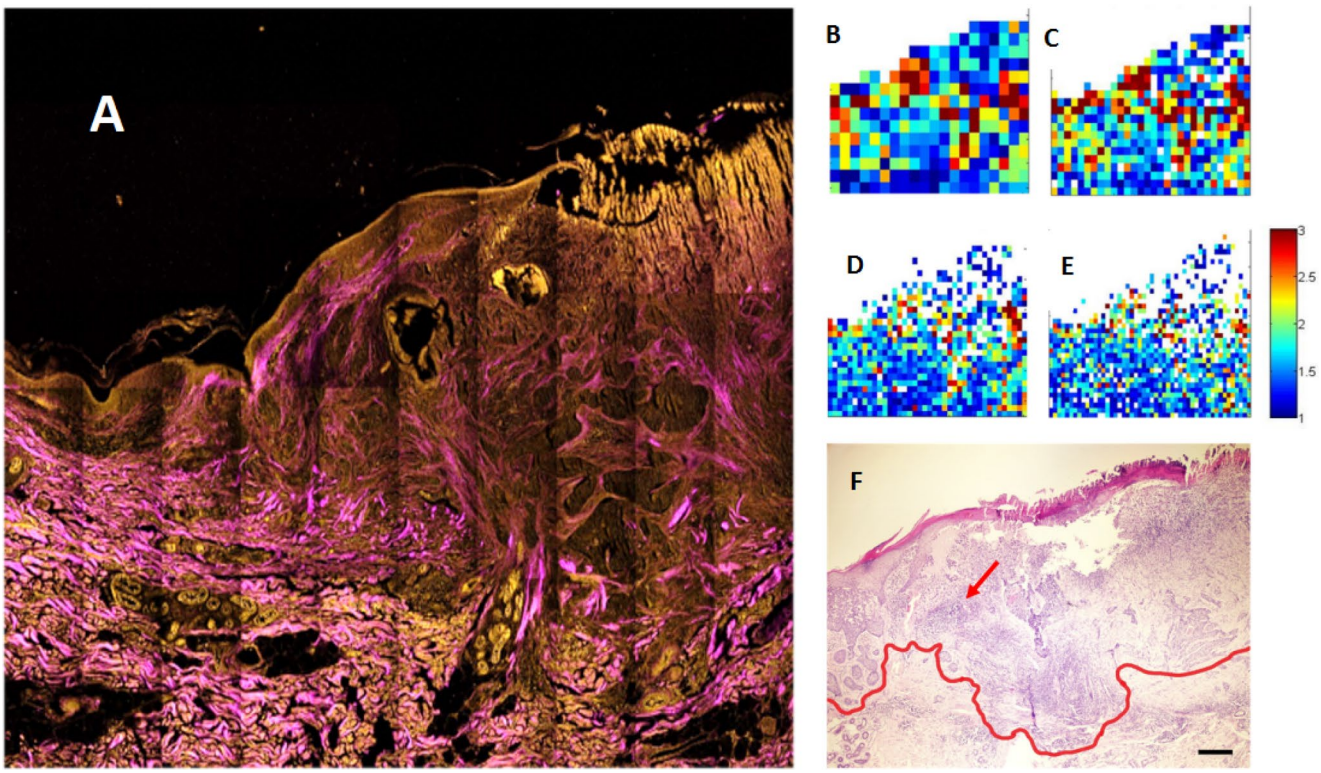

Fig. 1 Stain-free two-photon emission fluorescence (2PEF, orange) and second-harmonic generation (SHG, magenta) mosaic image of a deparaffinized nodular basal cell cancer section. For the imaging, a fiber coupled ~ 20 MHz repetition rate, tunable, sub-ps Ti: sapphire laser (FemtoRose TUN LC GTI, R&D Ultrafast Lasers Ltd., Budapest, Hungary) was used with an ~ 800 nm central wavelength. To capture the SHG signal of collagen (magenta), a 405/20 nm emission filter was used, for the 2PEF signal of keratin (orange), a 590/40 nm bandpass filter was used. (**A**) Mosaic image size: 4.2 mm x 4.2 mm. (B-E) Heatmaps (collagen orientation (CO) ratio maps) calculated for different spatial resolution. An individual NLM image was divided into (**B**): 2×2, (**C**): 3×3, (**D**): 4×4, (**E**): 5×5 even quadrangles (unit cells) for FFT analysis to determine CO ratio maps. Higher CO corresponds to collagen around the tumor, lower CO indicates healthy connective tissue. (**F**) Corresponding hematoxylin and eosin stained histopathological image. Red line: tumor border, red arrows: BCC nest. Scale bar displays 200 µm

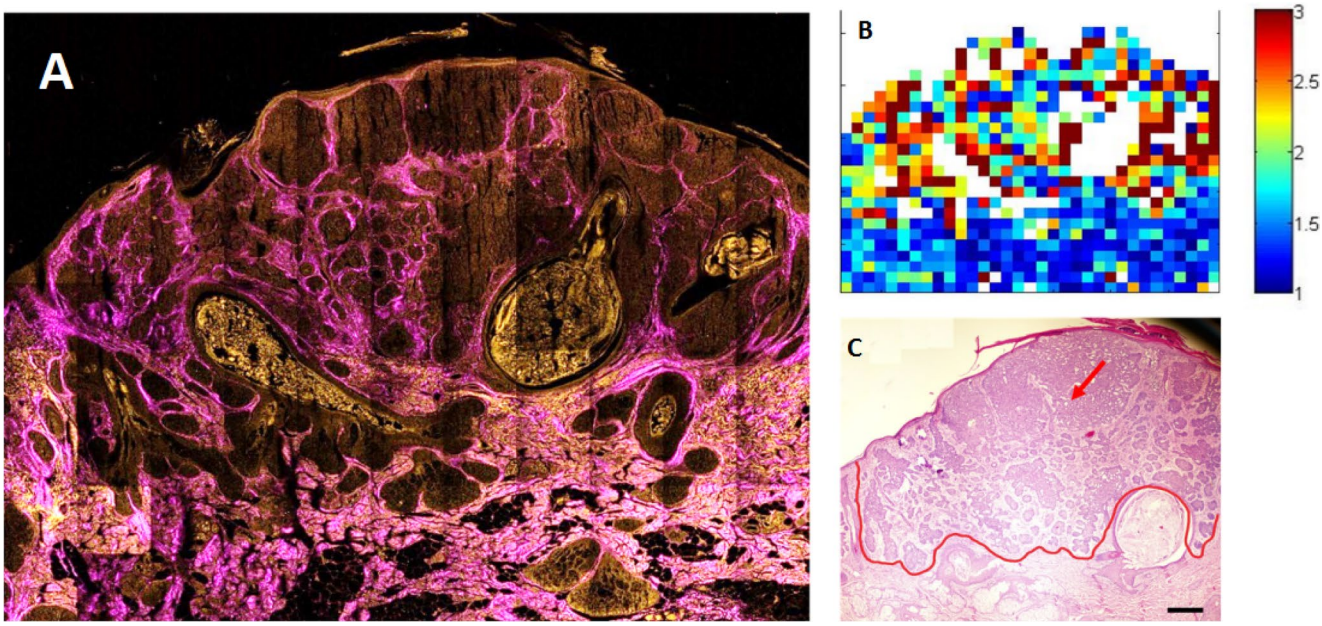

Fig. 2 Stain-free two-photon emission fluorescence (2PEF, orange) and second-harmonic generation (SHG, magenta) mosaic image of a deparaffinized micronodular basal cell cancer section. Imaging setup is the same as in case of Fig. 1. (**A**) Mosaic image size: 4.62 mm x 3.78 mm. Individual image size in mosaic image: 420 × 420 μm^2. (**B**) Corresponding heatmap of collagen orientation (CO) index with every field of view divided into 3 × 3 even quadrangles. Higher corresponds to collagen around the tumor, lower CO indicates healthy connective tissue. (**C**) Corresponding hematoxylin and eosin stained histopathological image. Red line: tumor border, red arrows: BCC nest. Scale bar displays 200 μm

Discussion

In this paper, we investigated the collagen fiber structure of nodular, micronodular and infiltrative BCC in order to delineate tumor borders. SHG and 2PEF signals of BCC skin sections were captured. Mosaic images underwent FFT analysis and the acquired collagen orientation index was used for contour delineation to identify the regular districts from the BCC regions. As collagen fibers in healthy skin are wavier, whereas around tumor nests these are more parallelly organized, numerical analysis of FFT images revealed higher long axis/short axis ratio in BCC samples around tumor nests compared to the healthy dermis. This higher CO leads to a numerical delineation of the tumor boundary, that was visualized on a heatmap. However, we experienced some artefacts that have to be considered during evaluation of these numerical results. We found that accuracy of FFT analysis highly depends on the unit cell size parameters (resolution, physical dimension of rectangular image portions) used for FFT. The higher the resolution of the analysis - smaller size of a distinct unit cell that underwent FFT -, the more challenging it was to distinguish between benign and malignant areas. This was due to the fact that the wavy character of collagen in the healthy dermis is lost, if it is evaluated in smaller unit cells. Thus, further analyses are needed to establish the most suitable size of the examined units. Also, for thinner collagen fibers, the analysis appeared to be less accurate. This posed challenges especially in case of nodular BCCs, where collagen fibers around the tumor nest appeared to be considerably thinner than in healthy collagen bundles. Finally, cross-sectional images of hair follicles and sebaceous glands and surrounding collagen fibers are prone to misinterpretation due to their similarly organized orientation to those around smaller tumor nests. As SHG imaging itself does not provide information on cellular structure. However, combination with 2PEF imaging proved to be helpful as it gives additional information on cellular morphology, so distinguishing between basal cell cancer cells and adnexal structures becomes feasible.

During our experiments, we provided an algorithm to mathematically analyze differences of collagen structure between the healthy dermis and around BCC tumor nests and to turn these results into visual information. Our findings indicate that the tumor microenvironment, including the organization of collagen networks may serve as a quantitative biomarker of the presence of BCC. The higher collagen orientation observed at the tumor boundary is a result of the extracellular matrix remodeling induced by local tumor growth [13]. On the contrary, an isotropic collagen network with more randomly organized fibers in a healthy dermis results in lower CO. FFT analysis provides quantitative information of the tumor boundary, complementing morphological evaluation of conventional histopathology. In practice, such an approach could guide clinicians in the

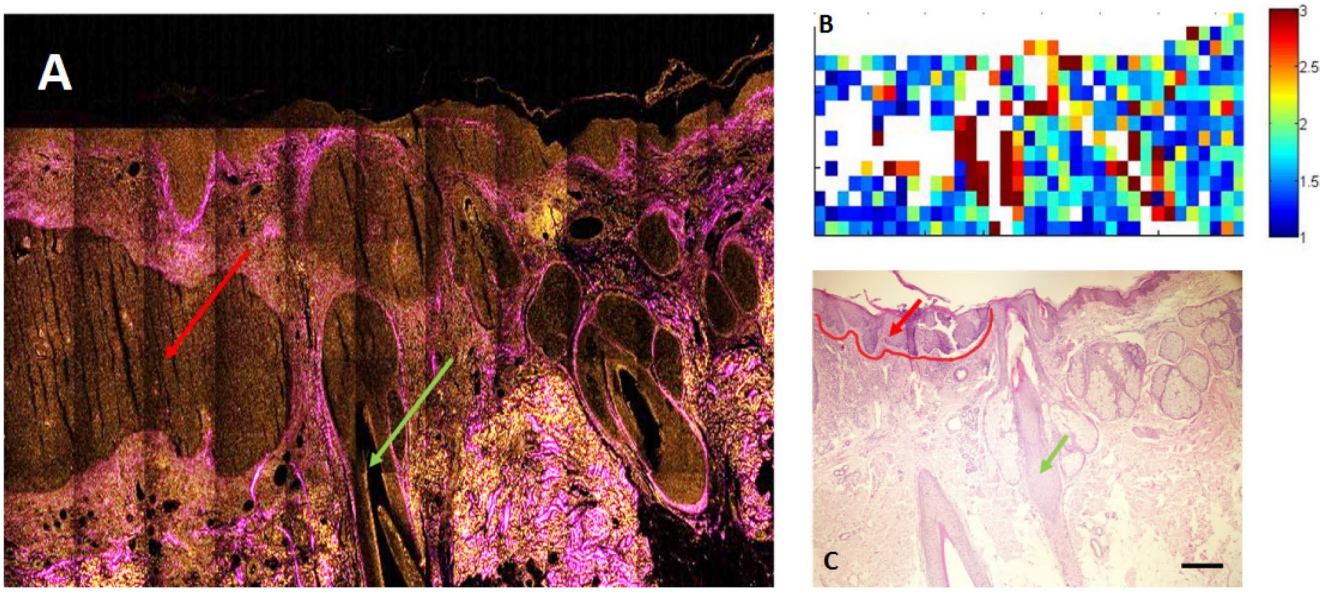

Fig. 3 Stain-free two-photon emission fluorescence (2PEF, orange) and second-harmonic generation (SHG, magenta) mosaic image of a deparaffinized micronodular basal cell cancer (BCC) section. Imaging setup is the same as in case of Fig. 1. This figure illustrates that collagen fibers around anatomical structures, such as around hair follicles can cause false positivity (**A**) Mosaic image size: 4.62 mm x 4.2 mm. Individual image size in mosaic image: 420 × 420 μm^2. (**B**) Corresponding heatmap of collagen orientation (CO) index with every field of view divided into 3 × 3 even unit cells. Higher corresponds to collagen around the tumor, lower CO indicates healthy connective tissue. (**C**) Corresponding hematoxylin and eosin stained histopathological image. Red arrow: BCC tumor nest, green arrow: hair follicle. Scale bar displays 200 μm

intraoperative identification of tumor margins in an objective, operator-independent way.

FFT has already been used to differentiate benign from malignant tissues according to the organization of collagen fibers in case of colorectal and breast cancer [13, 14]. They demonstrated that anisotropic collagen quantified by FFT indicates malignant dermal remodeling. Our results indicate that a similar principle is applicable to BCC despite its distinct growth pattern. As for BCCs, tumor margins are difficult to assess with dermoscopy, especially in case of the high-risk subtypes [2]. We experienced similar difficulties in the infiltrative subtype, but not in the micronodular, another high-risk subtype. Also, dermoscopic diagnostic criteria for BCCs are well known, however, distinctive features of different BCC types are still lacking. Only a few studies report on the dermoscopic features of micronodular BCCs, which highlight truncated vessels and multiple blue-gray globules [2]. Recently, clinical-dermoscopic characteristics of infiltrative BCCs were defined. Distinctive features included localization on the head and neck, a hypopigmented lesion with microulceration, shiny white structures and arborizing vessels as well as telangiectasia [15]. Previous studies on multiphoton imaging of BCC reported challenging identification of tumor regions or tumor-stromal interface [6, 7]. Our study demonstrates that quantitative SHG-based FFT analysis of collagen organization improves objective delineation of tumor borders. Combination with 2PEF provides complementary information that enables reliable morphological identification of the tumor regions and other dermal structures. These results are in agreement with our previous observations of increased collagen alignment around BCC nests [5]. The present study extends these qualitative observations by providing an automated quantitative methodology for tumor border identification.

To date, a routinely used imaging tool in the daily clinical practice for the diagnosis of BCC is dermoscopy, which provides a 10-fold magnification and inbuilt illumination. This cost-effective method increases diagnostic accuracy by 5–30% over visual inspection [16]. The polarized or non-polarized light penetrates through the stratum corneum until the dermis, and information from the epidermis, as well as the types of vessels in the upper dermis can be revealed. However, it is not suitable to establish a diagnosis due to its limited imaging depth and resolution. Other imaging techniques are primarily rather used in experimental settings. These include optical coherence tomography (OCT) which typically operates with near-infrared light that penetrates until the dermis. The interference pattern can be used in the diagnosis of skin cancer or to assess activity of inflammatory skin diseases. Its penetration is higher than in case of nonlinear optical microscopy, but the lateral resolution is usually lower [17]. Reflectance confocal microscopy (RCM) operates with a laser beam in the near-infrared range. The contrast is created by the different refractive

indices of the intra- and extracellular structures. Similarly to NLM, a resolution similar to conventional histopathology can be achieved and images parallel to the skin surface are obtained [18]. An advantage of NLM compared with ex vivo RCM is chemical selectivity. Combination of different NLM modalities result in multi-colored images, where different colors correspond to distinct structures. Besides SHG and 2PEF that visualize molecules and macromolecules, it can be supplemented with dual vibrational-resonance frequency (DVRF)-CARS imaging that visualizes different chemical bonds in a label-free manner. The resolution of NLM is similar to that of conventional histopathology reaching 400 μm beyond the skin surface [19, 20].

Our study has several limitations inherent to its small sample size and the pilot study design. Another limitation is that due to the 0.2–0.4 mm imaging depth, in vivo tumor assessment is not feasible with our imaging setup. Due to the application of distinct devices and softwares, it is yet not suitable for perioperative diagnosis, small field of view (0.4×0.4 mm^2) and relatively slow data collection (due to high resolution) limits imaging speed. Collagen thickness was not assessed, although this may increase the accuracy of delineation. We could not provide a reliable tool for quantitative differentiation of adnexal structures from tumor nests. Further research is needed to optimize imaging and analytical parameters and to investigate its applicability in routine clinical practice.

Still, FFT analysis of 2PEF and SHG images poses an alternative to DVRF-CARS imaging, that also yields stain-free imaging, similar to H&E staining, but is intricate, costly and challenging to implement at an industrial scale [9, 21]. These imaging modalities can be integrated in handheld nonlinear microscope systems [22], comprising a fiber-coupled, cost efficient sub-ps laser source operating at around 800 nm [21], for intraoperative application. Such methods are much needed for a fast and reliable tumor margin assessment. With intraoperative imaging of the excised skin samples, pathological analysis could be executed promptly, surgical accuracy could be increased, and reoperation rate could be reduced.

Acknowledgements The authors thank Enikő Kuroli for her help with the preparation of the skin sections and Lajos Vass for laser and microscope software development.

Author contributions Conceptualization: LF, RSZ. Data curation: LF, FM, AB, RSZ. Formal analysis: LF, RSZ. Funding acquisition: RSZ, NMW. Investigation: FM, LF, AB, RSZ. Methodology: RSZ. Resources: RSZ. Supervision: RSZ, NMW. Visualization: LF. Writing—original draft: LF, RSZ. Writing—review and editing: FM, AB, NMW, RSZ. All authors have read and approved the final manuscript.

Data availability The data that support the findings of this study are available from the corresponding author upon request.

Declarations

Consent for publication Patients signed informed consent regarding publishing their data.

Consent to participate Written informed consent was obtained from all subjects involved in the study.

Clinical trial number Not applicable.

Competing interests The authors declare no competing interests.

References

1. Verkouteren JAC, Ramdas KHR, Wakkee M, Nijsten T (2017) Epidemiology of basal cell carcinoma: scholarly review. Br J Dermatol 177(2):359–372. https://doi.org/10.1111/bjd.15321
2. Álvarez-Salafranca M, Ara M, Zaballos P (2022) Dermoscopy in Basal Cell Carcinoma: An Updated Review. Actas Dermosifiliogr 113(6):330–338. https://doi.org/10.1016/j.adengl.2021.01.023
3. Aref MH, El-Gohary M, Elrewainy A, Mahmoud A, Abougha-leb IH, Hussein AA, El-Ghaffar SA, Mahran A, El-Sharkawy YH (2023) Emerging technology for intraoperative margin assessment and post-operative tissue diagnosis for breast-conserving surgery. Photodiagn Photodyn Ther 42:103507. https://doi.org/10.1016/j.pdpdt.2023.103507
4. Ibrahim HM, Aref MHF, Elhadad MK, Hussein AA, Sharawi A, Saleh N (2026) MEMS-based near-infrared spectroscopy with AI for real-time breast cancer margin assessment. Surg Oncol 66:102395. https://doi.org/10.1016/j.suronc.2026.102395
5. Kiss N, Haluszka D, Lorincz K, Gyongyosi N, Bozsanyi S, Banvolgyi A, Szipőcs R, Wikonkál N (2019) Quantitative Analysis on Ex Vivo Nonlinear Microscopy Images of Basal Cell Carcinoma Samples in Comparison to Healthy Skin. Pathol Oncol Res 25(3):1015–1021. https://doi.org/10.1007/s12253-018-0445-1
6. Balu M, Zachary CB, Harris RM, Krasieva TB, König K, Tromberg BJ et al (2015) In Vivo Multiphoton Microscopy of Basal Cell Carcinoma. JAMA Dermatol 151(10):1068–1074. https://doi.org/10.1001/jamadermatol.2015.0453
7. Vogler N, Meyer T, Akimov D, Latka I, Krafft C, Bendsoe N et al (2010) Multimodal imaging to study the morphochemistry of basal cell carcinoma. J Biophotonics 3(10–11):728–736. https://doi.org/10.1002/jbio.201000071
8. Surkov YI, Serebryakova IA, Kuzinova YK, Konopatskova OM, Safronov DV, Kapralov SV, Genina EA, Tuchin VV (2024) Multimodal Method for Differentiating Various Clinical Forms of

Basal Cell Carcinoma and Benign Neoplasms In Vivo. Diagnostics (Basel Switzerland) 14(2):202. https://doi.org/10.3390/diagnostics14020202
9. Krolopp Á, Fésűs L, Szipőcs G, Wikonkál N, Szipőcs R (2024) A 20 MHz Repetition Rate, Sub-Picosecond Ti-Sapphire Laser for Fiber Delivery in Nonlinear Microscopy of the Skin. Life (Basel) 14(2). https://doi.org/10.3390/life14020231
10. Ayres C, Bowlin GL, Henderson SC, Taylor L, Shultz J, Alexander J et al (2006) Modulation of anisotropy in electrospun tissue-engineering scaffolds: Analysis of fiber alignment by the fast Fourier transform. Biomaterials 27(32):5524–5534. https://doi.org/10.1016/j.biomaterials.2006.06.014
11. Osman OS, Selway JL, Harikumar PE, Stocker CJ, Wargent ET, Cawthorne MA et al (2013) A novel method to assess collagen architecture in skin. BMC Bioinformatics 14(1):260. https://doi.org/10.1186/1471-2105-14-260
12. Munisso MC, Saito S, Tsuge I, Morimoto N (2023) Three-dimensional analysis of load-dependent changes in the orientation of dermal collagen fibers in human skin: A pilot study. J Mech Behav Biomed Mater 138:105585. https://doi.org/10.1016/j.jmbbm.2022.105585
13. Despotović SZ, Milićević ĐN, Krmpot AJ, Pavlović AM, Živanović VD, Krivokapić Z et al (2020) Altered organization of collagen fibers in the uninvolved human colon mucosa 10 cm and 20 cm away from the malignant tumor. Sci Rep 10(1):6359. https://doi.org/10.1038/s41598-020-63368-y
14. Falzon G, Pearson S, Murison R (2009) Analysis of collagen fibre shape changes in breast cancer. Phys Med Biol 53:6641–6652. https://doi.org/10.1088/0031-9155/53/23/001
15. Pampena R, Parisi G, Benati M, Borsari S, Lai M, Paolino G et al (2020) Clinical and Dermoscopic Factors for the Identification of Aggressive Histologic Subtypes of Basal Cell Carcinoma. Front Oncol 10:630458. https://doi.org/10.3389/fonc.2020.630458
16. Davis S, Piggott C, Lyon C, DeSanto K (2020) Effectiveness of dermoscopy in skin cancer diagnosis. Can Fam Physician 66(10):739–740
17. Sattler E, Kästle R, Welzel J (2013) Optical coherence tomography in dermatology. J Biomed Opt 18(6):061224. https://doi.org/10.1117/1.JBO.18.6.061224
18. Filoni A, Alaibac M (2019) Reflectance Confocal Microscopy in Evaluating Skin Cancer: A Clinicians's Perspective. Front Oncol 9:1457. https://doi.org/10.3389/fonc.2019.01457
19. Haluszka D, Lorincz K, Kiss N, Szipocs R, Kuroli E, Gyongyosi N et al (2016) Diet-induced obesity skin changes monitored by in vivo SHG and ex vivo CARS microscopy. Biomed Opt Express 7(11):4480–4489. https://doi.org/10.1364/BOE.7.004480
20. Szipőcs G, Krolopp Á, Chong SP, Török P, Szipőcs R (2023) Low Reflection Loss Dispersion Compensation Scheme for Broadly Tunable sub-ps Solid State Lasers. CLEO 2023, Technical Digest Series (Optica Publishing Group), JTh2A.121. https://opg.optica.org/abstract.cfm?URI=CLEO_FS-2023-JTh2A.121
21. Fésűs L, Krolopp Á, Molnár G, Kiss N, Tamás G, Szipőcs R (2020) A 20 MHz, sub ps, Tunable Ti:sapphire Laser System for Real Time, Stain Free, High Contrast Histology of the Skin. In: Biophotonics Congress: Biomedical Optics 2020, 20 April 2020, Washington, DC: Optica Publishing Group. https://opg.optica.org/abstract.cfm?URI=Microscopy-2020-MTh3A.4
22. Krolopp A, Csakanyi A, Haluszka D, Csati D, Vass L, Kolonics A, Wikonkál N, Szipőcs R (2016) Handheld nonlinear microscope system comprising a 2 MHz repetition rate, mode-locked Yb-fiber laser for in vivo biomedical imaging. Biomed Opt Express 7(9):3531–3542. https://doi.org/10.1364/BOE.7.003531